SAND2007-1977C

Verification for Multi-Mechanics Applications

Stefan P. Domino*
Sandia National Laboratories, Albuquerque, NM, 87185-0385

Greg Wagner †
Sandia National Laboratories, Livermore, CA, 94551-0969

Anay Luketa-Hanlin ‡
Sandia National Laboratories, Albuquerque, NM, 87185-1135

Amalia Black §
Sandia National Laboratories, Albuquerque, NM, 87185-0828

James Sutherland ¶
University of Utah Department of Chemical Engineering, Salt Lake City, UT 84112

Verification and validation of software in the field of scientific computing is increasingly being recognized as a critical part of the software, algorithm, and model development cycle. Multi-mechanics coupling represents an important and challenging role in providing confidence in the integrated multi-mechanics codes. This paper presents an overview of the math models implemented within the Sandia National Laboratories Advanced Simulation and Computing SIERRA Mechanics code project that supports the engulfed object-in-a-fire scenario. This scenario is characterized by coupling turbulent fluid mechanics, combustion, soot generation and transport, participating media radiation (PMR), thermal conduction and in the case of propellant fires, reacting Lagrangian particles. Attaining an adequate state of code verification for such a complex engineering mechanics scenario represents a daunting challenge. A systematic approach is therefore required. Examples of single and multiple mechanics verification methodologies will be presented.

Nomenclature

u	velocity, m/s
ρ	Density, kg/m^3
p	Pressure, N/m^2
τ_{ij}	Viscous stress tensor, kg/m-s^2
μ	Viscosity, kg/m-s
h	Enthalpy, kJ/kg
q	Heat flux, W/m^2
Pr	Prandtl number

*Principal Member of the Technical Staff, Thermal/Fluid Computational Engineering Sciences, Sandia National Laboratories, P.O. Box 5800, Mail Stop 0382, Albuquerque, NM, 87185-0382

†Principal Member of the Technical Staff, Thermal/Fluid Engineering Sciences, Sandia National Laboratories, P.O. Box 969, Mail Stop 9409, Livermore, CA, 94551-0969

‡Senior Member of the Technical Staff, Fire Science and Technology Department, Sandia National Laboratories P.O. Box 5800, Mail Stop 1135, Albuquerque, NM, 87185-1135

§Senior Member of the Technical Staff, Verification and UQ Processes, Sandia National Laboratories, P.O. Box 5800, Mail Stop 0828, Albuquerque, NM, 87185-0828

¶Assistant Professor, Department of Chemical Engineering, 50 South Campus Drive MEB Rm 3290, Salt Lake City, UT, 84112

Sc Schmidt number
Y Mass fraction
ω Reaction rate, kg/s-m^3
D Diffusion coefficient, m^2/s
T Temperature, K
Q Volumetric heating, W/m^3
k Thermal conductivity, W/m-K
C_p Specific heat, kJ/kg-K
Subscript
i Component
t Turbulent
p Particle
$\circ$ Reference condition

I. Introduction

The objective of this paper is to present several different solutions suitable for verification of multi-mechanic applications using a suite of computational codes, Fuego, Calore, and Syrinx, developed at Sandia National Laboratories. These application codes are built within the SIERRA framework which provides data structures, scalable parallelism, and a common interface for modern linear and nonlinear solvers, all within a fully unstructured mesh environment. Additionally, code coupling is naturally supported via surface and volume transfers (currently done via linear interpolation) on potentially non-conformal meshes. In utilizing the SIERRA framework, these codes can be coupled to solve a variety of multi-mechanic applications which involve heat transfer between fluid/fluid, fluid/solid and fluid/solid/PMR regions. Systematic code and solution verification has been carried out using these coupled suite of codes for various models using a variety of techniques including: code-code comparisons, similarity solutions, boundary layer solutions, exact solutions, and the method of manufactured solutions.

The objective of code verification is to reveal coding mistakes that affect the order of accuracy and to determine if the governing discretized equations are being solved correctly. Quite often, the process of verification reveals algorithmic issues that would otherwise remain unknown. For example, detailed time accuracy verification studies has provided further understanding of stabilized finite volume methods.[1]

In practice, a variety of comparison techniques exist for verification. For example, benchmark and code-to-code comparison is not considered rigorous due to the errors that exist in other code solutions, such as from discretization and iteration. Analytic solutions and the method of manufactured solutions remain the most powerful methods for code verification, since they provide a means to obtain quantitative error estimations in space and time.

Roache[2–4] has made the distinction between code verification and calculation verification, where calculation verification involves grid refinement required for every problem solution to assess the magnitude, not order, of the discretization error. Discretization errors, distinguished from modeling and iteration errors, is defined as the difference between the exact solution to the continuum governing equations and the solution to the algebraic systems representation due to discretization of the continuum equations. The order of accuracy can be determined by comparing the discretization error on successively refined grids. Thus, it is desirable to have an exact solution for comparision to determine the discretization errors.

The problems of interest to this project typically involve fire/object interaction applications that represents a set of transport equations that are coupled via surface or volume terms. For example, participating media radiation couples to the fluid mechanics via a volume term; the divergence of the radiative flux appears in the energy equation (see Eq. 11) for the fluids, while the temperature, emissivity, and absorption coefficients are required for the radiative transport equation, Eq. 26. In the case of a fluid-thermal conduction interface, coupling occurs via surface boundary conditions. The same applies for a radiation-solid interface. All of the couplings must be verified to be of the same order of accuracy as the discretizations used in each of the separate mechanics in order to maintain a consistent discretization scheme for the coupled problem.

The following paper first provides a description of the equation sets utilized within these codes and the methodology to solve the equations. Next, a description of the single mechanics verification problems and results are provided for analytical, semi-analytical and manufactured verification problems. When possible,

analytical solutions are used to verify the order of accuracy of the numerical scheme. However, the ability to use analytical solutions to verify a typical turbulence model implementation is not possible. Therefore, the method of manufactured solutions (MMS) is applied to a traditional two equation Reynolds Averaged Navier-Stokes (RANS) turbulence model verification study. In the case of multi-mechanics coupling, the use of analytical solutions is also limited. However, multi-mechanics verification using analytical solutions for a physics suite germane to the scenario of interest can be demonstrated. Examples of analytical solutions for the coupling of radiative transport and thermal conduction will be presented. In most cases, verification of multi-mechanics coupling must be demonstrated by the use of the MMS. The use of the method of manufactured solutions for a conjugate heat transfer verification study will be presented. This study is especially useful towards understanding the introduced numerical error when coupling through non-conformal and, possibly, disparate topological meshes. Techniques to verify the Lagrangian/Eulerian particle/fluid mechanics coupling will also be presented. Such verification test range from simple terminal velocity calculations to detailed momentum coupling between the Lagrangian and Eulerian field. The ability to demonstrate verification between a turbulent flow field and particle dispersion is demonstrated by comparing analytical particle spreading rates with the computed spreading rates.

Using a systematic verification approach starting with single mechanics verification and ending with multi-mechanics coupling verification can provide a resonable level of confidence in a multi-mechanics simulation tool. However, completing a full verification plan for a multi-mechanics code project such as Fuego/Calore/Syrinx represents a time consuming, challanging task. This paper, therefore, represents a current state of verification with current algorithmic implementations openly presented. Verification represents an ongoing effort for the combined project.

II. Equation Set

II.A. Fluid Mechanics

The equations that describe a turbulent reacting flow follow.

II.A.1. Continuity

$$\frac{\partial \bar{\rho}}{\partial t} + \frac{\partial}{\partial x_j}\bar{\rho}\tilde{u}_j = 0, \tag{1}$$

II.A.2. Momentum

The Favre-filtered momentum equations used for turbulent transport are

$$\frac{\partial \bar{\rho}\tilde{u}_i}{\partial t} + \frac{\partial \bar{\rho}\tilde{u}_i\tilde{u}_j}{\partial x_j} = -\frac{\partial p}{\partial x_i} + \frac{\partial \bar{\tau}_{ij}}{\partial x_j} + \frac{\partial \tau_{u_i u_j}}{\partial x_j} + (\bar{\rho} - \rho_\circ)\, g_i, \tag{2}$$

where the turbulent stress $\tau_{u_i u_j}$ is defined as

$$\tau_{u_i u_j} \equiv -\bar{\rho}(\widetilde{u_i u_j} - \tilde{u}_i\tilde{u}_j). \tag{3}$$

For RANS simulations, $\tau_{u_i u_j}$ represents the Reynolds stress tensor and can be reduced to the form $\tau_{u_i u_j} = -\overline{\rho u_i'' u_j''}$ by substitution of the Favre decomposition $u_i \equiv \tilde{u}_i + u_i''$ for each variable and simplifying. The deviatoric (trace-free) part of the stress tensor is defined as

$$\begin{aligned} \tau^D_{u_i u_j} &\equiv \tau_{u_i u_j} - \frac{1}{3}\tau_{u_k u_k}\delta_{ij} \\ &= \tau_{u_i u_j} + \frac{2}{3}\bar{\rho}\tilde{k}\delta_{ij} \end{aligned} \tag{4}$$

where the turbulent kinetic energy is defined as $\tilde{k} \equiv \frac{1}{2}\widetilde{u_k'' u_k''}$. The deviatoric part of the Reynolds stress tensor is modeled by the Boussinesq approximation which relates the Reynolds stresses to the filtered strain

rate tensor through a modeled turbulent viscosity μ_t, resulting in

$$\begin{aligned} \tau^D_{u_i u_j} &= \mu_t \left(\frac{\partial \tilde{u}_i}{\partial x_j} + \frac{\partial \tilde{u}_j}{\partial x_i} \right) - \frac{2}{3} \mu_t \frac{\partial \tilde{u}_k}{\partial x_k} \delta_{ij} \\ &= 2\mu_t \left(\tilde{S}_{ij} - \frac{1}{3} \tilde{S}_{kk} \delta_{ij} \right), \end{aligned} \tag{5}$$

where the filtered strain rate tensor is defined by

$$\tilde{S}_{ij} \equiv \frac{1}{2} \left(\frac{\partial \tilde{u}_i}{\partial x_j} + \frac{\partial \tilde{u}_j}{\partial x_i} \right). \tag{6}$$

Substituting this into Equation 4 yields the modeled form of the full Reynolds stress tensor (Kuo,[5] p. 445)

$$\tau_{u_i u_j} = 2\mu_t \left(\tilde{S}_{ij} - \frac{1}{3} \tilde{S}_{kk} \delta_{ij} \right) - \frac{2}{3} \bar{\rho} \tilde{k} \delta_{ij}. \tag{7}$$

For LES, $\tau_{u_i u_j}$ in Equation 2 represents the subgrid stress tensor. The deviatoric part of the subgrid stress tensor is defined as

$$\begin{aligned} \tau^D_{u_i u_j} &\equiv \tau_{u_i u_j} - \frac{1}{3} \tau_{u_k u_k} \delta_{ij} \\ &= \tau_{u_i u_j} + \frac{2}{3} \bar{\rho} q^2 \delta_{ij}, \end{aligned} \tag{8}$$

where the subgrid turbulent kinetic energy is defined as $q^2 \equiv \frac{1}{2}(\widetilde{u_k u_k} - \tilde{u_k}\tilde{u_k})$.

The subgrid turbulent kinetic energy is then modeled similar to RANS closures as

$$\tau_{u_i u_j} = 2\mu_t \left(\tilde{S}_{ij} - \frac{1}{3} \tilde{S}_{kk} \delta_{ij} \right). \tag{9}$$

In general, the Fuego simulation tool supports a variety of turbulence models including: RANS models, e.g. standard k-ϵ, low Reynolds k-ϵ, v^2-f model of Durbin; and LES models, K_{sgs}, and the static and dynamic coefficient Smagorinsky model. For purposes of this verification paper, the model of interest, which will not be explitely outlined, is the standard k-ϵ RANS model with wall functions.

II.A.3. Conservation of Energy

The integral form of the Favre-filtered energy equation, here shown for static enthalpy, used for turbulent transport is

$$\frac{\partial \bar{\rho} \tilde{h}}{\partial t} + \frac{\partial \bar{\rho} \tilde{h} \tilde{u}_j}{\partial x_j} = -\frac{\partial \bar{q}_j}{\partial x_j} - \frac{\partial \tau_{h u_j}}{\partial x_j} - \frac{\partial \bar{q}^r_i}{\partial x_i} \tag{10}$$

$$+ \frac{Dp}{Dt} + \bar{\tau}_{ij} \frac{\partial \tilde{u}_j}{\partial x_j}. \tag{11}$$

When the low Mach number equation set is in use, the last two terms of the above equation are neglected. The participating media radiation coupling is provided by the flux divergence term, $\frac{\partial \bar{q}^r_i}{\partial x_i}$.

When a simple Fickian diffusion velocity approximation is assumed the mean diffusive heat flux vector $\bar{q}_j$ is

$$\bar{q}_j = -\overline{\left[\frac{\mu}{\mathrm{Pr}} \frac{\partial h}{\partial x_j} - \frac{\mu}{\mathrm{Pr}} \sum_{k=1}^{K} h_k \frac{\partial Y_k}{\partial x_j} \right]} - \overline{\frac{\mu}{\mathrm{Sc}} \sum_{k=1}^{K} h_k \frac{\partial Y_k}{\partial x_j}}. \tag{12}$$

If Sc = Pr, i.e., unity Lewis number (Le = 1), then the diffusive heat flux vector simplifies to $\bar{q}_j = -\frac{\mu}{\mathrm{Pr}} \frac{\partial \tilde{h}}{\partial x_j}$.

The turbulent diffusive flux vector $\tau_{h u_j}$ in Eq. 11 is defined as

$$\tau_{h u_j} \equiv \bar{\rho} \left(\widetilde{h u_j} - \tilde{h} \tilde{u}_j \right). \tag{13}$$

For RANS simulations, τ_{hu_j} represents the turbulent energy diffusive flux vector and is simplified to the form $\tau_{hu_j} = \overline{\rho h'' u_j''}$ by substitution of the Favre decomposition of each variable. It is then modeled by

$$\tau_{hu_j} = \overline{\rho h'' u_j''} = -\frac{\mu_t}{\mathrm{Pr}_t}\frac{\partial \tilde{h}}{\partial x_j}, \tag{14}$$

where Pr_t is the turbulent Prandtl number and and μ_t is the modeled turbulent eddy viscosity from momentum closure. For LES, τ_{hu_j} represents the subgrid turbulent energy diffusive flux vector, and is modeled in the same way as

$$\tau_{hu_j} = -\frac{\mu_t}{\mathrm{Pr}_t}\frac{\partial \tilde{h}}{\partial x_j}, \tag{15}$$

where Pr_t is the subgrid turbulent Prandtl number and μ_t is the modeled subgrid turbulent eddy viscosity from momentum closure.

The resulting filtered and modeled turbulent energy equation for both RANS and LES is given as

$$\begin{aligned} \frac{\partial \bar{\rho}\tilde{h}}{\partial t} + \frac{\partial \bar{\rho}\tilde{h}\tilde{u}_j}{\partial x_j} &= \frac{\partial}{\partial x_j}\left(\frac{\mu}{\mathrm{Pr}} + \frac{\mu_t}{\mathrm{Pr}_t}\right)\frac{\partial \tilde{h}}{\partial x_j} - \frac{\partial \bar{q}_i^r}{\partial x_i} \\ &+ \frac{\partial p}{\partial t} + \tilde{u}_j\frac{\partial p}{\partial x_j} + \bar{\tau_{ij}}\frac{\partial \tilde{u}_j}{\partial x_j}. \end{aligned} \tag{16}$$

II.A.4. Conservation of Species

The Favre-filtered species equation used for turbulent transport is

$$\frac{\partial \bar{\rho}\tilde{Y}_k}{\partial t} + \frac{\partial \bar{\rho}\tilde{Y}_k\tilde{u}_j}{\partial x_j} = -\frac{\partial \tau_{Y_k u_j}}{\partial x_j} - \frac{\partial \overline{\rho Y_k \hat{u}_{j,k}}}{\partial x_j} + \overline{\dot{\omega}_k}, \tag{17}$$

where the form of diffusion velocities $\hat{u}$ assumes the Fickian approximation with a constant value of diffusion velocity for consistency with the turbulent form of the energy equation, Eq. 11, i.e., $\hat{u}_{j,k} = -\frac{D}{Y_k}\frac{\partial}{\partial x_j}Y_k$.

The turbulent diffusive flux vector $\tau_{Y_k u_j}$ is defined as

$$\tau_{Y_k u_j} \equiv \bar{\rho}\left(\widetilde{Y_k u_j} - \tilde{Y}_k\tilde{u}_j\right). \tag{18}$$

For RANS simulations, $\tau_{Y_k u_j}$ represents the turbulent species diffusive flux vector and is simplified to the form $\tau_{Y_k u_j} = \overline{\rho Y_k'' u_j''}$ by substitution of the Favre decomposition of each variable. It is then modeled as

$$\tau_{Y_k u_j} = \overline{\rho Y_k'' u_i''} = -\frac{\mu_t}{\mathrm{Sc}_t}\frac{\partial \tilde{Y}_k}{\partial x_i}, \tag{19}$$

where Sc_t is the turbulent Schmidt number for all species and μ_t is the modeled turbulent eddy viscosity from momentum closure. For LES, $\tau_{Y_k u_j}$ represents the subgrid turbulent species diffusive flux vector, and is modeled identically as

$$\tau_{Y_k u_j} = -\frac{\mu_t}{\mathrm{Sc}_t}\frac{\partial \tilde{Y}_k}{\partial x_i}, \tag{20}$$

where Sc_t is the subgrid turbulent Schmidt number for all species and μ_t is the subgrid modeled turbulent eddy viscosity from momentum closure.

The Favre-filtered and modeled turbulent species transport equation for both RANS and LES then becomes,

$$\frac{\partial \bar{\rho}\tilde{Y}_k}{\partial t} + \frac{\partial \bar{\rho}\tilde{Y}_k\tilde{u}_j}{\partial x_j} = \frac{\partial}{\partial x_j}\left(\frac{\mu}{\mathrm{Sc}} + \frac{\mu_t}{\mathrm{Sc}_t}\right)\frac{\partial \tilde{Y}_k}{\partial x_j} + \overline{\dot{\omega}}_k. \tag{21}$$

If transporting both energy and species equations, the laminar Prandtl number must be equal to the laminar Schmidt number and the turbulent Prandtl number must be equal to the turbulent Schmidt number to maintain unity Lewis number. Although there is a species conservation equation for each species in a

mixture of K species, only $K-1$ species equations need to be solved since the mass fractions sum to unity and

$$\tilde{Y}_k = 1 - \sum_{j \neq k}^{K} \tilde{Y}_j. \tag{22}$$

Finally, a variety of reaction models, e.g., Magnussun's Eddy Dissipation Concept (EDC) used to close the mean reaction rate, $\overline{\dot{\omega}}$. The alternative to tracking a set of species transport equations is to compute a conserved scalar, Z, that is defined by the following transport equation,

$$\frac{\partial \bar{\rho}\tilde{Z}}{\partial t} + \frac{\partial \bar{\rho}\tilde{Z}\tilde{u}_j}{\partial x_j} = \frac{\partial}{\partial x_j}\frac{\mu_t}{\mathrm{Sc}_t}\frac{\partial \tilde{Z}}{\partial x_j}, \tag{23}$$

subject to the appropriate initial and boundary conditions, e.g. $\tilde{Z} = 1$ at a fuel inlet and $\tilde{Z} = 0$ elsewhere.

II.B. Thermal Conduction

Thermal conduction is provided by the standard conduction equation,

$$\rho C_p \frac{\partial T}{\partial t} + \frac{\partial q_j}{\partial x_j} = \dot{q} \tag{24}$$

where q_j represents the heat flux vector, here shown in the limiting case of isotropic thermal conductivity, k,

$$q_j = -k\frac{\partial T}{\partial x_j} \tag{25}$$

and$\dot{q}$ represents the volumetric heating source term.

II.C. Participating Media Radiation

The spatial variation of the radiative intensity corresponding to a given direction and at a given wavelength within a radiatively participating material, $I(s)$, is governed by the Boltzmann transport equation. In general, the Boltzmann equation represents a balance between absorption, emission, out-scattering, and in-scattering of radiation at a point.

With the assumptions of negligible scattering and very fast reaction time scales, the appropriate form of the filtered Botzmann radiative transport equation for sooting hydrocarbon diffusion flames is

$$s_i \frac{\partial}{\partial x_i} I\left(s\right) + \bar{\mu}_a I\left(s\right) = \overline{\mu_a I_b}, \tag{26}$$

where μ_a is the absorption coeffiecient, $I(s)$ is the intensity along the direction s_i and I_b is the blackbody intensity at temperature T,

$$I_b = \frac{\sigma T^4}{\pi} \tag{27}$$

The closure of the mean emissive power, $\overline{\frac{\mu_a \sigma T^4}{\pi}}$, is provided through the EDC model or the presumed pdf mixture fraction model via standard turbulent radiation interation techniques.

The flux divergence may be written as a difference between the radiative emission and mean incident radiation at a point,

$$\frac{\partial q_i^r}{\partial x_i} = \mu_a \left[4\sigma T^4 - G\right], \tag{28}$$

The radiation intensity must be defined at all portions of the boundary along which $s_i n_i < 0$, where n_i is the outward directed unit normal vector at the surface. The intensity is applied as a Dirichlet condition which must be determined from the surface properties and temperature. The diffuse surface assumption provides reasonable accuracy for many engineering combustion applications; the intensity leaving a diffuse surface in all directions is given by

$$I\left(s\right) = \frac{1}{\pi}\left[\tau\sigma T_\infty^4 + \epsilon\sigma T_w^4 + \left(1 - \epsilon - \tau\right)H\right], \tag{29}$$

where H is the surface irradation.

II.D. Lagrangian Particle Transport

II.D.1. Particle momentum

The equations of motion for a particle with constant mass moving through a fluid are simply

$$\dot{\mathbf{x}}_p = \mathbf{v}_p \tag{30}$$
$$m_p \dot{\mathbf{u}}_p = \mathbf{F}_p(\mathbf{u}_p(t), t) \tag{31}$$

where m_p, $\mathbf{x}_p$, $\mathbf{u}_p$ are the particle mass, position and velocity, and $\mathbf{F}_p$ is the total force on the particle. We assume that the total force is the drag plus a constant external force (e.g. due to gravity):

$$\mathbf{F}_p(\mathbf{u}_p, t) = \mathbf{F}_{drag}(\mathbf{v}_p, t) + \mathbf{F}_{ext}. \tag{32}$$

The drag force can be written in terms of the drag coefficient C_D:

$$\mathbf{F}_{drag}(\mathbf{v}_p, t) = -\frac{3 m_p \rho_f C_D v_{rel}}{8 \rho_p R_p}(\mathbf{v}_p - \mathbf{v}_f) \tag{33}$$

where ρ_f is the fluid density, ρ_p is the particle density, R_p is the particle radius, and $\mathbf{v}_f$ is the fluid velocity. The relative velocity v_{rel} is the magnitude of the velocity difference between the particle and fluid:

$$v_{rel} = |\mathbf{v}_p - \mathbf{v}_f|. \tag{34}$$

For a spherical particle, the drag coefficient is modeled as

$$C_D = \begin{cases} 24(1 + Re^{2/3}/6)/Re & \text{for } Re < 1000 \\ 0.424 & \text{for } Re >= 1000 \end{cases} \tag{35}$$

where the particle Reynolds number Re is given by

$$Re = \frac{2 \rho_f R_p v_{rel}}{\mu_f}; \tag{36}$$

μ_f is the fluid viscosity

II.D.2. Particle energy

The energy equation solved for a Lagrangian particle assumes a two-temperature model: a core particle temperature T_p, and a "film" temperature T_f at the particle surface. The change in particle internal energy is then the sum of heat conduction between the gas at temperature T_g and the film, and net radiative heat transfer:

$$m_p C_{v,p} \dot{T}_p = 2\pi N u_f R_p k_f (T_g - T_f) + \pi \epsilon R_p^2 (G - 4\sigma T_f^4) \tag{37}$$

where $C_{v,p}$ is the particle specific heat, Nu_f and k_f are the Nusselt number and thermal conductivity at the film, and σ is the Stefan-Boltzmann constant. The equation can be closed by solving for the film temperature that balances internal heat transfer between the core and film temperatures with the external heat transfer, given by the right-hand side of (37). The Nusselt numbers both inside and outside the particle are obtained from empirical relations that are functions of the particle and fluid properties.[6]

II.E. Coupled Mechanics Conditions

II.E.1. Thermal Conduction Coupled Boundary Condition

The thermal conduction boundary condition, in the presence of both fluid flow and participating media radiation, is given by

$$q_n = -k \frac{\partial T}{\partial x_j} n_j = h(T - T^r) + \epsilon \left(\sigma T^4 - H \right) \tag{38}$$

where h is the heat transfer coefficient and T^r is the reference temperature (each computed by the fluids solver); H, the surface irradiation, is computed by Syrinx.

The coupling between the thermal conduction region and the fluids and PMR region is through the computed wall temperature. This wall temperature is used to compute the intensity boundary condition, Eq. 29. The computed wall temperature from the thermal conduction region is also used to compute the heat flux from the wall to the fluid.

II.E.2. Fluid and PMR Coupling

The volumetric coupling between the fluids region and PMR region is through the flux divergence term, Eq. 28. This term is linearized to provide a left hand side contribution to the enthalpy transport equation,

$$\frac{\partial}{\partial T}\frac{\partial q_i^r}{\partial x_i}\Delta T = \frac{\partial}{\partial T}\bar{\mu}_a\left[4\sigma T^4 - G\right]\frac{\Delta h}{C_p} \tag{39}$$

$$= 16\mu_a T^3\frac{\Delta h}{C_p}, \tag{40}$$

The coupling between the PMR region and the fluids region is through providing the absorption coefficient $\bar{\mu}_a$ and the mean emisive power, $\frac{\overline{\mu_a \sigma T^4}}{\pi}$ shown in Eq. 26.

II.F. Fluid-Particle-PMR Coupling

The effects of the Lagrangian particles on the fluid are incorporated through source terms on the fluid momentum and energy equations. Sources are obtained by summing point source contributions from all particles:

$$\mathbf{S}_{mom} = \sum_P (\mathbf{F}_{ext} - m_p\dot{\mathbf{u}}_p)\delta(\mathbf{x}_P - \mathbf{x}) \tag{41}$$

$$\mathbf{S}_{energy} = \sum_P \left(-m_p C_{v,p}\dot{T}_p - Q_{rad,p}\right)\delta(\mathbf{x}_P - \mathbf{x}) \tag{42}$$

where $\delta(\mathbf{x})$ is the Dirac delta function, and $Q_{rad,p}$ is the net radiative flux on particle p (the last term on the right-hand side of Eqn. 37). The contribution from $Q_{rad,p}$ is subtracted because radiation from the particle does not directly affect the local fluid energy; rather, the particle contributes to the absorption coefficient and source terms in the participating media radiation equation (26).

III. Numerical Methodologies

III.A. Turbulent Fluid Mechanics

The SIERRA Mechanics module resposible for the solution of the turbulent reacting fluid mechanics is Fuego. Fuego uses the finite volume technique known as the control volume finite element method. Control volumes (the mesh dual) are constructed about the nodes. Each element contains a set of subfaces that define control-volume surfaces. The subfaces consist of line segments (2-D) or surfaces (3-D). The 2-D segments are connected between the element centroid and the edge centroids. The 3-D surfaces are connected between the element centroid, the element face centroids, and the edge centroids. Integration points also exist within the subcontrol volume centroids. Such integration points are used for volume integrals such as source terms, the mass matrix, and, if chosen, gradients. Heterogenous topological elements including hexahedral, tetrahedral, wedges and pyramids are supported.

An approximate projection method[1] is used to solve the coupled continuity/momentum system. A Picard solution strategy is the solution choice to converge the set of nonlinear equations within the fluids mechanics region.

III.B. Thermal Heat Conduction

The SIERRA Mechanics module resposible for the solution of the thermal conduction object response is Calore. Calore uses a standard Galerkin finite element method.[7] For the purposes of this paper, enclosure radiation, chemistry and mesh adaptivity will not be outlined or considered.

III.C. Participating Media Radiation

The SIERRA Mechanics module resposible for the solution of the radiative transport equation is Syrinx. Syrinx employs a streamwise upwind Petrov-Galerkin finite element method discretization for the method of discrete ordinates.[8] The degree of local stabilization is controled by a comparison between the cell size and optical thickness.

IV. Verification Tests

IV.A. Analytical

Analytical problems are defined by exact solutions to the governing equations of interest. In general, the use of analytical solutions are limited to isothermal, uniform laminar flow. Nevertheless, use of analytical solutions can provide confidence in the core numerical method.

IV.A.1. 1x1 Fully Developerd Laminar Flow

A classic analytical solution for a 1x1 fully developed parabolic laminar flow in a two dimensional rectangular channel of height H is given by,

$$u(y) = -\frac{1}{2\mu}\frac{dP}{dx}\left(yH - y^2\right). \tag{43}$$

This parabolic closed solution is easily derived based on the boundary conditions that $u(y=0)=0$ and $u(y=H)=0$ along with $\frac{dp}{dx} = constant$ and $u = f(y), v = w = 0$. A numerical scheme that is second order will reproduce the analytical result exactly to machine precision. For the conditions of $H = 0.5\ m$, $\mu =$ 1.e-3 kg/m-s and $\frac{\partial P}{\partial x} = 0.048$ Pa/m, the analytic centerline velocity (at $y = H/2$) is 1.5 m/s. Figure 1 illustrates the streamwise velocity as a function of channel height for a uniform refinement study using a MUSCL convection operator with symmetry planes. In each simulation, the difference between the analytical and computed solution was machine precision.

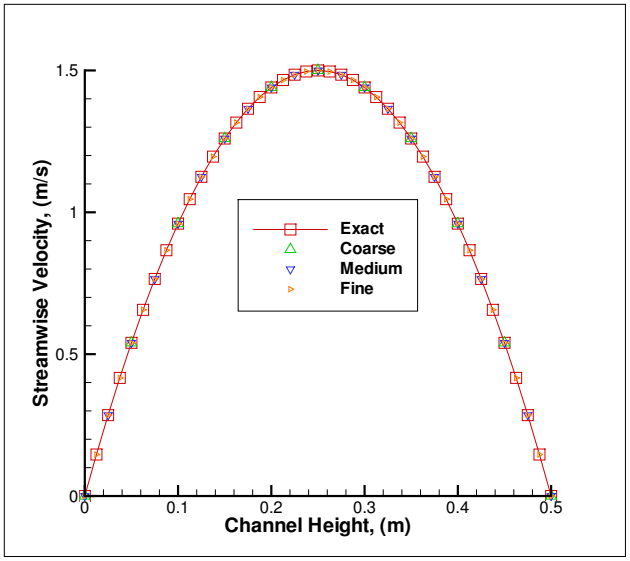

Figure 1. Comparision between analytical and computed solution on three meshes using the MUSCL operator.

IV.B. Semi-Analytical

Semi-analytical solutions are defined as those that exist as an unclosed analytical form, e.g. infinite series. The problem used to showcase semi-analytical solutions for laminar isothermal flow is provided by Berker.[9] The geometry was selected to be a channel rectangular channel of width 1 m, height 2 m, and length 20 m.

The material properties are a fluid with a density of 1E-3 kg/m^3 and a viscosity of 1E-4 kg/m. A specified pressure drop is provided to be 1.60e-3 Pa/m.

The axial velocity distribution is

$$v = -\frac{1}{2\mu}\frac{dp}{dz}\left[b^2 - y^2 - \frac{4}{b}\sum_{n=0}^{\infty}(-1)^n \frac{1}{m^3}\frac{\cos(my)\cosh(mx)}{\cosh(ma)}\right] \tag{44}$$

where

$$m = \frac{(2n+1)\pi}{2b} \tag{45}$$

The half-width in the x-direction is a and the half-width in the y-direction is b. The axial direction down the duct is z.

The centerline velocity, at $x = y = 0$, is provided by

$$v(0,0) = -\frac{1}{2\mu}\frac{dp}{dz}\left[b^2 - \frac{4}{b}\sum_{n=0}^{\infty}(-1)^n \frac{1}{m^3}\frac{1}{\cosh(ma)}\right]. \tag{46}$$

Computing the first 1000 terms of the above series provides a centerline velocity of 1.82195.

Three meshes, starting at 32e3 elements and uniformly refined to 256e3 and 2.048e6 elements were run. Errors in the centerline velocity as a function of normalized mesh spacing are shown in table 1. The apparant order of accuracy is just above 2.0.

Table 1. Error norms for centerline velocity with hybrid MUSCL scheme.

	Δ	v(0,0)
L_∞	1.0	5.70686e-4
	0.5	1.40686e-4
	0.25	4.06860e-05

A study was also performed in which the coarse mesh was arbitrarily rotated about the x, y and z axis ($123^\circ, 25^\circ$ and 12°) and run to verify that the error in the computed centerline velocity remained exactly the same error (5.70686e-4). This simple test activates the non-orthogonal terms in each equation set and provides confidence in the tool when running flows that are not aligned with the principle set of axis.

IV.C. Boundary Layer Solutions

Analytical solutions for the boundary layer equations can be useful as part of a verification study. One such problem is the buoyant plume above a line source Yih.[10] This simularity solution can be used to verify both the species and energy transport algorithm independently. Since this solution is not based on the full Navier-Stokes equations, problem parameters have to be specified such that the full flow equations approximate the boundary layer equations.

Error norms (L_∞) for the temperature equation, using a hybrid MUSCL convection operator scheme, are shown in table 2. These errors are relative to the boundary layer solution and indicate an order of accuracy of approximately 1.7. The computed order of accuracy is ambigous and suggests that a Richardson extrapolation technique might be required due to the differences between the Navier-Stokes solution and the boundary layer solution.

Table 2. Error norms for temperature equation with hybrid MUSCL scheme; errors are relative to the boundary layer solution.

	Δ	T
L_∞	1.0	3.52309e-01
	0.5	1.40779e-01
	0.25	4.75744e-02
	0.125	1.95432e-02

IV.D. Method of Manufactured Solutions

The method of manufactured solutions represents a powerful manner in which the order of accuracy of a method can be determined. The idea is to assume a solution field in the domain of interest and then apply the governing differential operators to the given solution set. Since this solution set typically does not satisfy the governing equations, extra source terms arise, which must be added into the code. Thus, a modified set of the governing equations result where all terms can be evaluated exactly. The resulting simulation result should converge to the manufactured solution.

A simple example, in the context of three dimensional heat conduction, to illustrate this technique is provided by the manufactured solution,

$$T(x, y, z) = \cos(a\kappa x)\sin(b\kappa y)\sin(c\kappa z) \tag{47}$$

where a = 3, b = c = 2; and $\kappa = \pi$. This equation is substituted into the steady form of Eq. 24 to provide the following source term,

$$S_{mms}(x, y, z) = \left((a\kappa)^2 + (b\kappa)^2 + (c\kappa)^2\right)\left(\cos(a\kappa x)\sin(b\kappa y)\sin(c\kappa z)\right) \tag{48}$$

Figure 2 shows the order of accuracy plot for the Fuego conduction region refinement case using a non orthogonal t-hex mesh with the full control volume finite element diffusion stencil. In this verification study, the L_1 and L_2 norms are converging at a second order accuracy, whereas, the L_∞ norm is between first and second order.

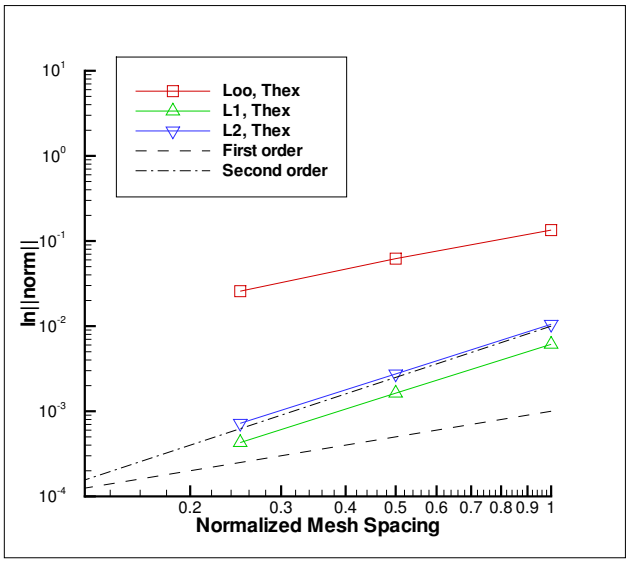

Figure 2. Plot of error vs normalized mesh spacing to demonstrate convergence of the Fuego method of outlined manufactured solution; results shown for the non orthogonal thex study with full CVFEM diffusion operator.

IV.D.1. Steady Two-Equation Turbulence Model

The following solution equations for velocity components and pressure is a modified solution taken from Ethier and Steinman.[11] This solution represents an exact 3-D transient solution to the Navier-Stokes equations. It has been modified to be steady for this manufactured solution test in order to test spatial accuracy. This solution also can be easily modified to a transiet solution set to test temporal accuracy (not shown in this paper). In this study, the domain is $-L \le x \le L, -M \le y \le M, -N \le z \le N$ where $L = M = N = 0.5$.

$$u(x, y, z) = -a[e^{ax}\sin(ay + dz) + e^{az}\cos(ax + dy)] \tag{49}$$
$$v(x, y, z) = -a[e^{ay}\sin(az + dx) + e^{ax}\cos(ay + dz)] \tag{50}$$
$$w(x, y, z) = -a[e^{az}\sin(ax + dy) + e^{ay}\cos(az + dx)] \tag{51}$$

In the above, $a = \frac{\pi}{4}, d = \frac{\pi}{2}$. Two pressure fields (case 1 and case 2) were tested:

$$p(x,y,z) = -\frac{1}{2}(u^2+v^2+w^2) \quad (52)$$

$$p(x,y,z) = \sin(c_1 x)\sin(c_2 y)\sin(c_3 z) \quad (53)$$

where $c_1 = \frac{\pi}{2L}, c_2 = \frac{\pi}{2M}, c_3 = \frac{\pi}{2N}$. The turbulent kinetic energy manufactured solution is given by,

$$k(x,y,z) = -\frac{3}{2}C_d d^2[e^{az}\sin(ax+dy) + e^{ax}\cos(ay+dz)] + C \quad (54)$$

where $C_d = 0.09$ and $C = 2$ (added to avoid negative values of k). The turbulence dissipation manufactured solution is given by,

$$\varepsilon(x,y,z) = \zeta k^2 \quad (55)$$

where the constant ζ is provided to balance the unit disparity.

The convergence plots for the L_2 norm for case 1 and case 2 are shown in figure 3. Note that for all cases the mesh spacing has been normalized to the 10^3 mesh, which corresponds to a mesh spacing of 1. Note that the pressure is expressed as $\hat{p} = p + \frac{2}{3}\bar{\rho}k$, where p is the true pressure. Thus, in order to compare pressure fields, $\frac{2}{3}\bar{\rho}k$ was added to the analytical pressure solution during post-processing. The computed pressure field can float by some constant, thus the pressure field was normalized by setting the computed pressure equal to the maximum value of the analytical solution at the same nodal location for all meshes. The amount substracted to make these values equivalent was then subtracted from all the other nodes. The residual norms dropped by twelve orders of magnitude for each mesh.

The results indicate that all velocity components, k, and ϵ approach second order behavior for the L_2 and infinity error norms (not shown). The pressure field is approaching second order behavior for the L_2 norms, however, not for the infinity norms (not shown).

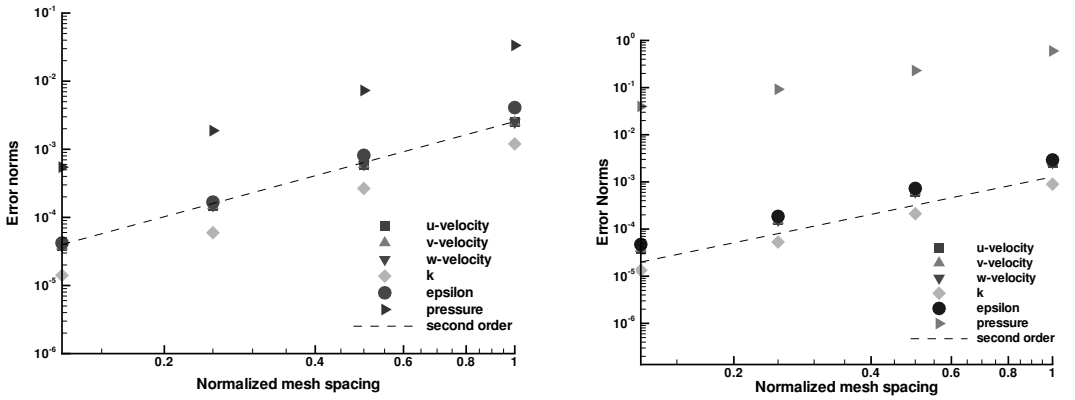

Figure 3. Plot of L2 error norms vs normalized mesh spacing for velocity components, k, epsilon, and pressure; Case 1 (L) and Case 2 (R)

V. Coupled Mechanics Verification

V.A. Analytical

V.A.1. Thermal/Radiation Coupling; Radiation Between Two Concentric Spherical Shells

Analytical solutions also exist for coupled mechanics problems of interest. Consider two concentric spheres with a gap between them. Within the gap is a vacuum, i.e., a non-participating media. The outer boundary of the outer shell, at radius $r_\circ$, is maintained at the temperature $T_\circ$ while the inner temperature at radius r_i is maintained at temperature T_i. An energy balance about the outer sphere, i.e., from $r_2 \leq r_\circ$, states that

the energy conducted through the outer shell must be equal to the energy radiated from the inner radius of the outer shell to the outer radius of the inner shell.

$$Q_\circ = 4\pi k_\circ \frac{r_2 r_\circ}{r_\circ - r_2}\left(T_2 - T_\circ\right) = A_2 \mathcal{F}_{12}\sigma\left(T_1^4 - T_2^4\right). \tag{56}$$

Likewise, an energy balance about the inner shell states that the heat conducted through the inner shell is equal to the energy radiated from the outer radius of the inner shell to the inner radius of the outer shell,

$$Q_i = 4\pi k_i \frac{r_1 r_i}{r_1 - r_i}\left(T_i - T_1\right) = A_1 \mathcal{F}_{12}\sigma\left(T_1^4 - T_2^4\right). \tag{57}$$

where k_i and $k_\circ$ are the inner and outer thermal conductivities and the exchange factor is defined as,

$$A_1\mathcal{F}_{12} = \frac{1}{\frac{\rho_i}{\epsilon_1 A_1} + \frac{1}{A_1} + \frac{\rho_2}{\epsilon_2 A_2}}. \tag{58}$$

The above energy balance relationships are solved for to provide the two surface temperatures. Finally, the temperature variation within the two shells are given by a cylindrical solution of the steady heat conduction equation,

$$T(r) = T_2 + (T_\circ - T_2)\frac{(1/r_2 - 1/r)}{(1/r_2 - 1/r_\circ)}; r_2 \leq r_\circ \tag{59}$$

$$T(r) = T_i + (T_1 - T_i)\frac{(1/r_i - 1/r)}{(1/r_i - 1/r_1)}; r_i \leq r_1 \tag{60}$$

For the geometry of: $r_\circ = 0.1m$, $r_2 = 0.075m$ $r_1 = 0.05m$ and $r_i = 0.03m$, material properties of the thermal conductivity within both shells of $k_\circ = k_i = 52W/m - K$ (bronze) and surface properties of $\epsilon_1 = 0.8$ and $\epsilon_2 = 0.6$, $T_1 = 302.834$ while $T_2 = 599.291$.

Although this problem can be solved simply by coupling a thermal conduction solver and an enclosure radiation solver, in this example, we allow for the use of Syrinx to compute the irradiation and use the following surface boundary condition for the thermal conduction region,

$$q_n = -k\frac{\partial T}{\partial x_j}n_j = \epsilon\left(\sigma T^4 - H\right) \tag{61}$$

The results of the inner and outer temperature profile as a function of radial distance are shown in figure 4. This simulation represented a S_8 quadrature on a series of uniformly refined meshes (thermal heat conduction meshes were 23,048, 189,120 and 1,512,960 elements for coarse, medium and fine, respectively; while the PMR meshes were 13,024, 94,560 and 756,480 elements). Since these meshes represent uniform mesh refinements, some slight error due to geometry effects are expected. Moreover, the difficulty with a discrete ordinates method is that there exists a quadrature error that persists as the mesh is refined. In this simulation study, the L_∞ norm for the inner temperature difference is converging at order 1.83. Moreover, the error between the predicted and exact temperature difference for the inner ring is 0.15 percent.

V.A.2. Falling Particle

The momentum equation for Lagrangian particles can be tested by comparing the terminal velocity of a particle falling in a quiescent fluid with the analytical solution value. At terminal velocity, the drag force exactly balances the gravitational force. The drag coefficient can be computed from this force; from (35) the exact value of this coefficient, as a function of the Reynolds number, should be:

$$\frac{C_D Re}{24} = \begin{cases} 1 + Re^{2/3}/6 & \text{for } Re < 1000 \\ \frac{0.424}{24} Re & \text{for } Re >= 1000 \end{cases} \tag{62}$$

The drag coefficient C_D has been multiplied by $Re/24$ to obtain a value that remains finite as $Re \to 0$.

Particles of varying radii were dropped in a quiescent flow in a Fuego simulation. Figure 5 shows the the drag coefficient as a function of Reynolds number, compared with the exact value from equation (62). Computed results match the expected value exactly.

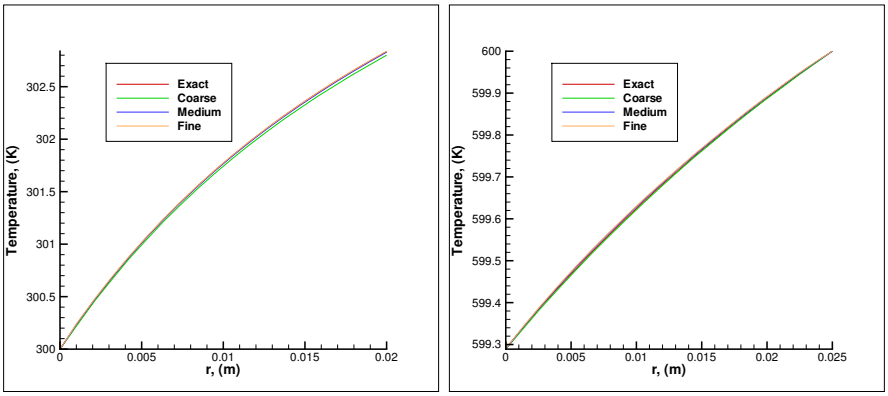

Figure 4. Plot of temperature profiles as a function of radial distance for exact, coarse, medium and fine meshes; inner (L) and outer (R)

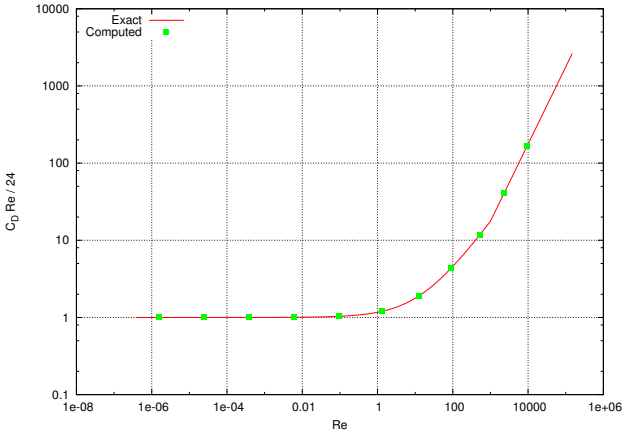

Figure 5. Drag coefficient computed from terminal velocity of falling particle as a function of Reynolds number.

V.A.3. Turbulent Dispersion of Particles

Lagrangian particles in a turbulent flow are exposed to random fluctuations in the fluid velocity. A particle in an isotropic, homogeneous turbulence field undergoes a random walk caused by the fluctuating drag forces that result. For a very small particle, i.e. with a velocity response time much smaller than the typical eddy lifetime, the variation in the particle position is given by

$$\langle (x - x_0)^2 \rangle = 2k\tau_e t \tag{63}$$

where k is the turbulent kinetic energy. The eddy lifetime τ_e is

$$\tau_e = \sqrt{\frac{3}{2}} \frac{C_\mu^{3/4} k}{\epsilon} \tag{64}$$

where ϵ is the turbulence dissipation and C_μ is a constant used in the k-ϵ turbulence model.

The Lagrangian particle implentation in Fuego was tested by placing a cloud of particles at $\mathbf{x} = \mathbf{0}$ in a homogeneous turbulence field, with constant k and ϵ, and measuring the mean square of the particle positions as a function of time. Results for various values of k and ϵ are plotted in figure 6 along with the analytical values. The dispersion of particles matches the expected analytical solutions.

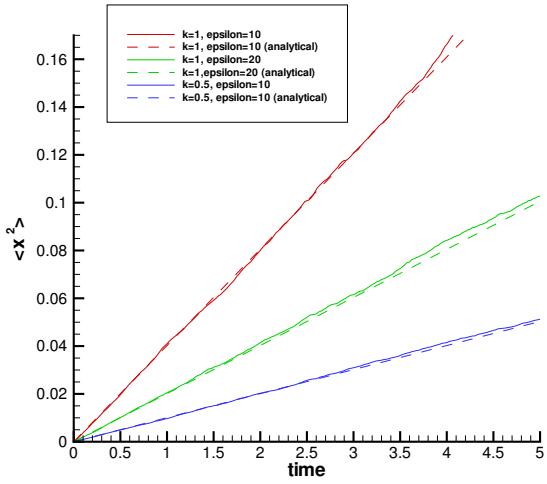

Figure 6. Dispersion of Lagrangian particles in a homogeneous turbulence field, compared with the analytical solution.

V.B. Manufactured Solutions

V.B.1. Conjugate Heat Transfer using the Method of Manufactured Solutions

The conjugate heat transfer (CHT) implementation in Fuego can be verified using MMS. A CHT problem is solved unit cube domain with the imposed manufactured solution given by:

$$T_{MMS}(x, y, z) = sin(3\pi x) sin(2\pi y) sin(2\pi z) + 2 \tag{65}$$

The unit cube domain is divided into two halves, with an interface at $x = 0$. The $x < 0$ half is a Fuego fluid region with zero flow field imposed, while the $x > 0$ half is a conduction-only region, so that in effect equation (24) is solved in both regions. Conjugate heat transfer is imposed at the interface, and a volumetric heating source term equal to $\nabla^2 T_{MMS}$ is included. Boundary conditions consistent with T_{MMS} are imposed at all boundaries other than the $x = 0$ interface.

The problem is solved to steady state, and the error is studied as a function of mesh size. The error converge for a uniform hexahedral mesh is plotted in figure 7. All measures of the error (L_∞, L_1, and L_2) show second order convergence, matching the formal order of accuracy for both individual regions.

However, two different effects can potentially lower this convergence rate. First, if a manufactured solution is chosen such that the derived source term does not go to zero at the interface, the convergence rate drops to first order; this is demonstrated in figure 8 for a manufactured solution of $T_{MMS} =$

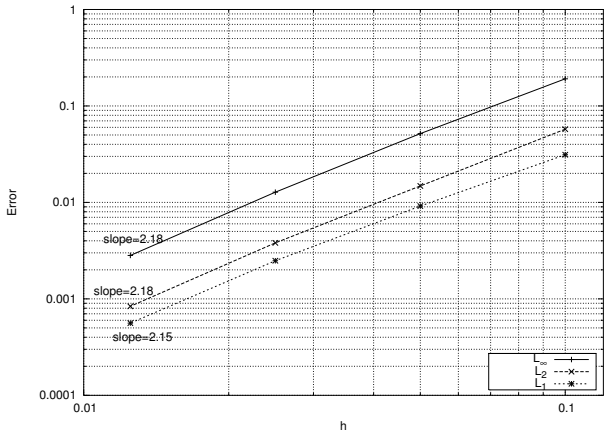

Figure 7. Convergence of CHT on a uniform hexahedral mesh. $T_{MMS} = sin(3\pi x)sin(2\pi y)sin(2\pi z) + 2$

$cos(3\pi x)sin(2\pi y)sin(2\pi z) + 2$. The drop in convergence rate is caused by the change in the way in which Dirichlet BC's are applied in a CVFEM method (using a lumped matrix approximation); energy conservation is lost on the control volumes at the interface, and a small part of the source term is neglected.

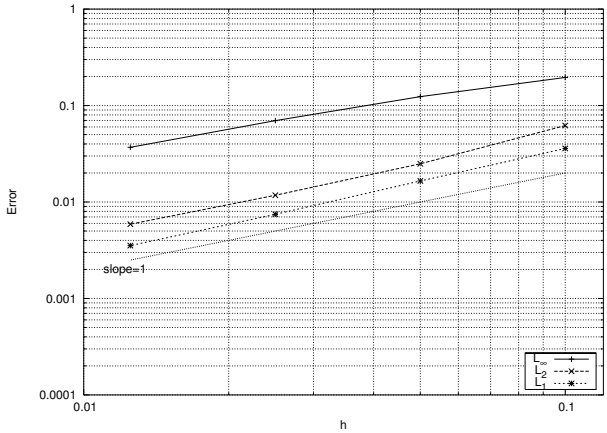

Figure 8. Convergence of CHT on a uniform hexahedral mesh. $T_{MMS} = cos(3\pi x)sin(2\pi y)sin(2\pi z) + 2$**, so that the derived MMS source term is non-zero at the** $x = 0$ **interface.**

We also find that convergence is affected if an unstructured tetrahedral mesh is used. Convergence is shown for two cases: one in which the meshes at the interface in the two regions are equivalent, i.e., conformal, and one in which the meshes at the surface do not match (figure 9). Convergence for both cases is only between first and second order. This loss of convergence appears to be due to the interpolation of the convection coefficients used to apply conjugate heat transfer on the conduction region surface.

This verification study of conjugate heat transfer demonstrates how difficult it can be to preserve the formal order of accuracy when multiple domains are coupled.

VI. Conclusion

In this paper, we have outlined a variety of problems which can be used for verification of multi-mechanic applications involving fluid and heat transfer coupling. A variety of techniques can be used to gain confidence that a code is solving the equations correctly and to determine order of accuracy, namely through code-code comparisons, similarity solutions, boundary layer solutions, exact solutions, and the method of manufactured solutions. The verifcation problem selection is based upon problems which exercise the physics expected to be important for the problems of interest. A group of verification problems can be selected which exercise a subset of the physics for an application, and taken collectively will exercise the physic set entirely. Verification and validation is a process which must be continually conducted for any computational code that undergoes

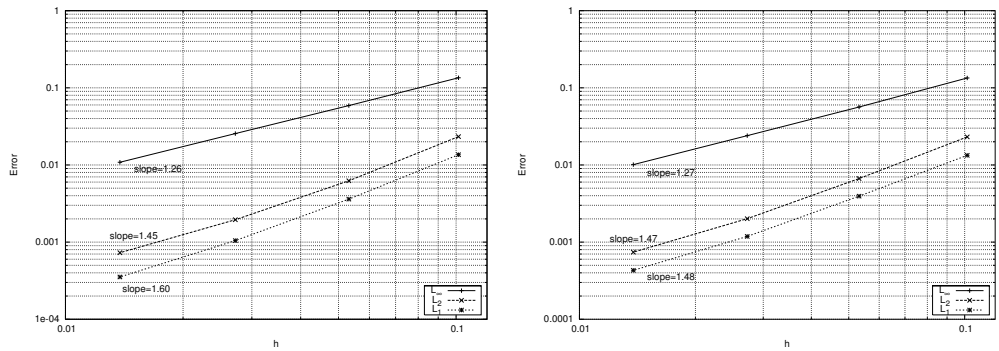

Figure 9. Convergence of CHT on tetrahedral meshes with matching (left) and non-matching (right) surface meshes at the interface.

continual research and development, such as is the case with the SIERRA/Calore/Fuego/Syrinx tool set.

Acknowledgments

Sandia is a multiprogram operated by Sandia Corporation, a Lockheed Martin Company for the United States Department Of Energys National Nuclear Security Administration under Contract DE-AC04-94AL85000.

References

[1]S.P. Domino, 'Toward verification of formal time accuracy for a family of approximate projection methods using the method of manufactured solutions', *Proceedings of the 2006 Summer Program, Center for Turbulence Research*, Vol. 11, pp. 163-177, 2006.

[2]Roache, P.J., 'Verification of Codes and Calculations', AIAA J., Vol. 36, No. 5, 1998.

[3]Roache, P.J., 'Code Verification by the Method of Manufactured Solutions', Trans. ASME, Vol. 124, 2002.

[4]Steinberg, S. and Roache, P.J., 'Symbolic Manipulation and Computational Fluid Dynamics', J.Comp. Phys., Vol. 57, No. 2, 1985.

[5]Kuo, K. K., *Principles of Combustion*, John Wiley and Sons, 1986.

[6]Sirignano, W.A., 'Fluid dynamics and transport of droplets and sprays,' Cambridge University Press, Cambridge, 1999.

[7]Reddy, J.N. and Gartling, D.K., *The Finite Element Method in Heat Transfer and Fluid Dynamics*, CRC Press, 2001.

[8]S.P. Burns, 'Applications of P Spatial and Angular Domain Based Parallelism to a Discrete Ordinates Formulation with Unstructured Spatial Discretization', *Prceedings of the Second International Symposium on Radiation Transfer*, pp. 173-193, 1997.

[9]Berker, R., 'Mouvement d'un fluide visqueux incompressible', Handbuch der Physik, Vol. 8, Part 2, Springer Verlag, Berlin, 1963.

[10]Yih, C., 'Laminar Free Convection Due to a Line Source of Heat', Transactions of the American Geophysics Union, Vol. 33, pp. 669-672, 1952.

[11]Ethier, C.R. and Steinman, D.A., 'Exact Fully 3D Navier-Stokes Solutions for Benchmarking', *Int. J. Numer. Methods Fluids*, Vol. 19, pp. 369-375, 1994.